


## Article

# Practical Design of a Low-Cost Icing Wind Tunnel for Unmanned Aerial Vehicle Testing in a Limited Space

Juan Carlos Plaza del Pino <sup>1,2,\*</sup>, Félix Terroba Ramírez <sup>1</sup> , Adelaida García-Magariño <sup>3</sup> , Ricardo Atienza Pascual <sup>1</sup> and Julio Mora Nogués <sup>4</sup>

<sup>1</sup> Escuela Politécnica Superior, Alfonso X el Sabio University (UAX), 28691 Madrid, Spain; fterrram@uax.es (F.T.R.); ratiepas@uax.es (R.A.P.)

<sup>2</sup> Doctoral Programme in Sciences (9601), National University of Education at Distance (UNED), 28015 Madrid, Spain

<sup>3</sup> Subdirección General de Sistemas Navales, National Institute of Aerospace Technology (INTA), 28048 Madrid, Spain; garciamga@inta.es

<sup>4</sup> Subdirección General de Sistemas Aeronáuticos, National Institute of Aerospace Technology (INTA), 28850 Madrid, Spain; jmornog@inta.es

\* Correspondence: jplaza73@alumno.uned.es

**Abstract:** Ice accretion on aircrafts due to atmospheric conditions is still a relevant research topic, especially in the case of Unmanned Aerial Vehicles (UAVs), due to their smaller size and the relative underdevelopment of ice protection systems (anti-icing and de-icing) for these aircraft. For the research and development of these systems, it is necessary to assess their performance in icing wind tunnels (IWTs), which are generally high-cost facilities. This article describes the design and building process of a new IWT for testing fixed-wing UAVs, aimed at cost reduction and restricted to an existing cold climate chamber of limited size. The designed IWT is an open-circuit type with two corners, a test section size of 0.40 m × 0.27 m and speed up to 70 m/s. The design process employs widely used and proven semi-empirical formulas, supported by detailed calculations using Computational Fluid Dynamics (CFD) tools, to achieve a test section core of useful quality and avoid flow separation. Theoretical limits with respect to a usable droplet size and Liquid Water Content (LWC) are calculated, and the test section core is estimated. The design process followed proves to be a very good approach to the design and aerodynamic optimisation of a low-cost IWT.

**Keywords:** icing wind tunnel; IWT; unmanned aerial vehicle; UAV; limited space; low cost; icing; design



**Citation:** Plaza del Pino, J.C.; Terroba Ramírez, F.; García-Magariño, A.; Atienza Pascual, R.; Mora Nogués, J. Practical Design of a Low-Cost Icing Wind Tunnel for Unmanned Aerial Vehicle Testing in a Limited Space. *Appl. Sci.* **2024**, *14*, 6928. <https://doi.org/10.3390/app14166928>

Academic Editor: Christos Bouras

Received: 17 July 2024

Revised: 5 August 2024

Accepted: 6 August 2024

Published: 7 August 2024



**Copyright:** © 2024 by the authors. Licensee MDPI, Basel, Switzerland. This article is an open access article distributed under the terms and conditions of the Creative Commons Attribution (CC BY) license (<https://creativecommons.org/licenses/by/4.0/>).

## 1. Introduction

Atmospheric icing remains an extremely important topic of study today, as it affects many sectors such as power generation [1,2], communications [3,4] and transport [5–7]. Martini et al. [1] published a comprehensive review on modelling icing in wind turbines, where they highlight the importance of paying special attention to the modelling of turbulence (as there is usually evidence of flow separation) and roughness. They also highlight the need for experimental studies to obtain reliable data to validate the models proposed in recent years, since these models have only been validated with other numerical results to date. However, they do note the difficulty in obtaining accurate experimental data and the need for the development of experimental measurement methods. In the communications sector, studies found in the literature address the problem of icing on overhead power transmission lines. These issues, as well as the main de-icing and anti-icing systems used in this field, can be found in recent reviews by Zhang et al. [3] and Li et al. [4]. Within the transport sector, although there are a considerable number of studies within the naval field, of which a summary of the main studies to date can be found in the review work of Zhou et al. [5], most studies belong to the aeronautics field [1].

The problem of icing in aeronautics is especially critical because it seriously affects the flight safety of aircraft [6,7]. According to Gultepe et al. [7], 30% of aviation accidents in the USA are due to weather conditions, one of those being icing conditions. And according to Jarosova et al. [8], 8% of accidents in the Czech Republic are due to ice accretion. The formation of ice on aerodynamic surfaces changes their geometry and behavior, thus degrading their aerodynamic performances and even potentially causing a stall, thereby seriously jeopardising their airworthiness. For example, Bromfield et al. [9] studied a recent in-flight accident relating to a tailplane stall due to icing. The current state of knowledge of the physics of icing and its mitigation in aviation can be found in the review works of Zhao et al. [10] and Yamazaki et al. [11]. According to Yamazaki et al. [11], the icing problem is still an active area of research due to its complexity, with the main focus of recent research being to understand the underlying physics of the problem, especially the “ice crystal” problem in engines (where studies in icing wind tunnel-type facilities are fundamental), as well as the development of ice mitigation methods.

To mitigate the effects of icing, manned aircraft are equipped with effective ice detection and protection systems, enabling them to fly through areas with icing clouds [12–17]. Recent advances in passive protection systems, using surfaces with different wettability [13] manufactured with new micro/nano fabrication methods [14] that improve the efficiency of such systems by up to twelve times, as well as the development of a new ice detection system based on “phase-transition-induced phosphorescence” recently published by Liu et al. [15], are noteworthy. New developments in photothermal anti-icing materials [17–19] are also remarkable. Recent advances in this field can be found in the review work of Wu et al. [20]. All these systems, in addition to the more traditional systems based on superhydrophobic coatings, thermoelectrics and piezoelectrics [21–24], are studied and validated in icing wind tunnel (IWT)-type installations. To this end, Yu et al. [25] have recently published a wind tunnel scaling method for aviation thermal anti-icing systems.

For Unmanned Aerial Vehicles (UAVs) the installation of new systems that add more weight or higher energy consumption [26] is more restricted in general, due to their smaller size and available power [27]. Therefore the technology of de-icing and anti-icing methods is much less developed. However, these aircrafts are increasingly used, and their development is undergoing an exponential increase. Increasing the flight autonomy and range of these aircrafts is therefore required to meet the requirements of the most demanding operations. In this context, ice detection and protection systems in UAVs will play a major role and enable them to fly safely in conditions for which they are currently unprepared, and for which the only mitigation measure available at present is flight cancellation. There is a need to develop and use detection and protection systems like those of manned aircraft, but adapted and sized to the capabilities and characteristics common to UAVs. In this situation, low-cost developments in UAVs are particularly important, as budget and resource constraints in this type of project are limiting factors when it comes to these new developments. Examples of low-cost UAV developments can be found in the work of Jiménez-Jiménez et al. [28] on UAV photogrammetry, Hu et al. [29] on a low-cost UAV Lidar system, Granados-Bolaños et al. [30] on a low-cost UAV applied to tropical volcanoes, Famiglietti et al. [31] on a low-cost UAV for positioning, Lussem et al. [32] on a low-cost UAV for forage mass monitoring, Schafaeer et al. [33] on a low-cost UAV for the study of hurricane damage or Liu et al. [34] on the study of CH<sub>4</sub> monitoring.

For the development of de-icing and anti-icing systems applied to UAVs, it is necessary to experimentally evaluate their behaviour in icing wind tunnels. Also, in the final phase of flight tests, when the new configurations are tested, it is necessary to demonstrate sufficient evidence in the wind tunnel tests to obtain the necessary flight authorisations. However, IWT-type facilities are generally expensive and costly, and are not commonly available at universities or smaller-scale centres, where such smaller UAV projects are conducted. This is why the development of a low-cost, small IWT could be vital in the development and adaptation of de-icing and anti-icing systems for UAVs.

Icing wind tunnels (IWTs) are complex facilities that allow the recreation of conditions such as those encountered in the icing that occurs during flight, and they are used both for more fundamental studies (to understand the underlying physics) and for more applied studies (the validation of de-icing and anti-icing technologies). An IWT differs from a general-purpose wind tunnel in that it has the ability to control temperature and misting conditions to simulate icing conditions, in addition to aerodynamic conditions relative to flight. It emulates velocity, temperature, water content and droplet or microdroplet size distribution, allowing it to reflect the specific conditions that are contained in CS-25 [35] Appendices C and O, on which the STANAG standards for Unmanned Aerial Systems (UAS) [36–38] are based.

There are many types of icing wind tunnels, more or less complex, but in general the functional parts that make up an IWT are as follows:

- Wind tunnel, responsible for accelerating the air and stabilising the required velocity in the test section, where the test specimen will be housed;
- Cooling system, responsible for reaching and maintaining the temperature required for the test, below the freezing temperature of water and normally below ambient temperature;
- Misting system, which generates and ejects water in the required quantity and droplet-size distribution.

There is a clearly defined classification according to the geometry of the wind tunnel and its associated cooling system: open-circuit tunnels inside freezing chambers or closed-circuit tunnels with a heat exchanger system. Figure 1 shows the two types of wind tunnels mentioned: the closed-circuit wind tunnel of the Alfonso X University (UAX), which currently has no cooling system and is therefore not an IWT (but the feasibility of converting it into an IWT could be studied in the future), and the current open-circuit IWT of INTA, with a test section of only  $15 \times 15 \text{ cm}^2$  and therefore a limited capacity in terms of the models to be tested. INTA's current IWT is limited to studies of anti-icing coatings and icing sensors on small test specimens or reduced-size models, allowing no aerodynamic testing to obtain forces.

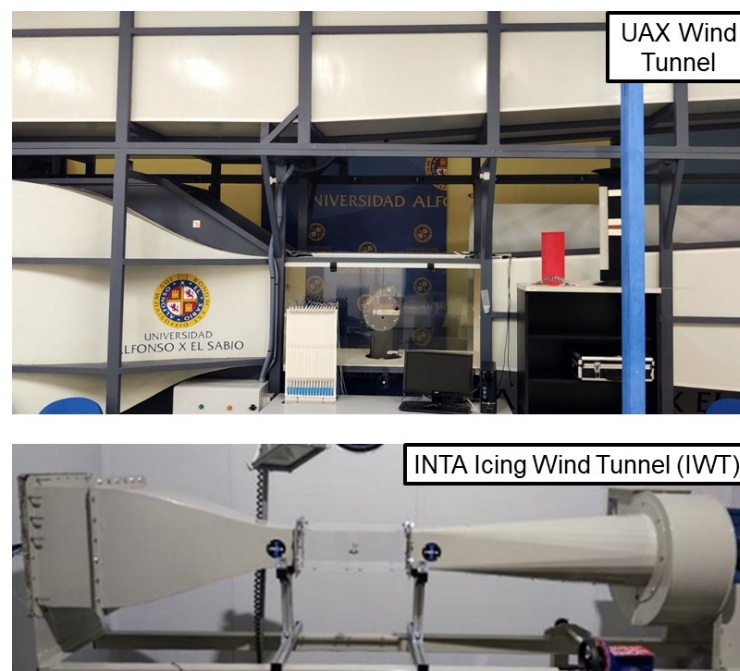


Figure 1. UAX wind tunnel and INTA icing wind tunnel (IWT).

In this context, the main objective of this paper is to show and describe the design process of a new low-cost open-circuit wind tunnel inside a freezing chamber, with a test section five times larger than the existing one at INTA, adapted for the evaluation of ice detection and ice protection systems in fixed-wing UAVs. This project will be constrained by several requirements:

- Adapting to an existing, small freezing chamber;
- Have a low cost;
- Meet the aerodynamic and size requirements for the test objective.

The outline of this paper can be summarised as follows: Section 2 presents the design process and its phases, Sections 3 and 4 describe the design process in detail and Section 5 shows the construction of the icing wind tunnel and its deviations. Finally, Section 6 summarises the main conclusions drawn.

## 2. Design Process Outline

The IWT design process has been based on a three-phase methodology (see Figure 2), similar to other design processes [39]. These phases consist of a preliminary design phase, verification and optimisation using Computational Fluid Dynamics (CFD) tools and final experimental validation tests after the IWT has been built. Validation tests could not be carried out, since the construction of the IWT has not been completed yet.

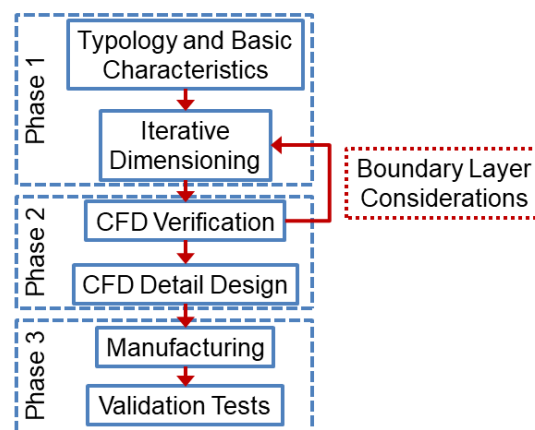


**Figure 2.** Phases of the design process.

### 2.1. Preliminary Design

The preliminary design consisted of the selection of the IWT typology, its basic characteristics and sizing, together with the required first approximation calculations. For this preliminary design, recommendations for the design of general-purpose wind tunnels have been followed [40–47], and the required calculations have been carried out for the use of wind tunnels in icing tests.

First of all, the existing space requirements and the objectives of the tunnel (the maximum speed to be reached) were defined, followed by the definition of the most basic characteristics of the IWT: type of circuit, type of test section, main dimensions of the test section, etc. Financial criteria have also been taken into account throughout the whole process.

Secondly, each of its sections has been defined in detail using the formulas obtained from the various studies on wind tunnel design [40]. These formulas are based on analytical one-dimensional models, experimentally corrected. These corrections and experimental adjustments are based on the abundant existing literature, and the model has been widely used in tunnel design for decades [48].

Given the existing restrictions on the overall dimensions, the design has consisted of an iterative process of successive refinements of the dimensions of the different sections (their areas and their lengths and conicities), so that the general tunnel design criteria are met, as well as the specific requirements of this case. This iterative process has allowed the geometry of the IWT to be optimised, while meeting the constraints.

In the case of any wind tunnel, the power required for its operation and its energy consumption are crucial. But this is especially so in the case of an IWT, due to the need to keep the air temperature low, for which any energy loss in the form of heat (from the operation of the fan and from the friction of the air passing through the circuit) will have to be compensated for by a cooling system.

For this reason, the design has been optimised for maximum efficiency (or minimum pressure drop to be compensated for by the fan), which means minimum aerodynamic heat loss. In an IWT, the minimum temperature that can be reached or the maximum test time is limited by the cooling system, which has to compensate not only for the heat losses of the refrigerated chamber itself, but also for the heat generated by the fan and air friction.

The pressure drop has been calculated for each of the sections and added together to give the total pressure drop in the tunnel. The dynamic pressure is determined by the law of continuity, so energy losses by components reduce the total pressure (and therefore the static pressure). The total pressure drop must be compensated for by the fan and is therefore related to the required fan power. In addition, it is needed, together with the flow rate, to define the fan.

The loss coefficient of each section can be defined as the ratio of the pressure loss in section  $\Delta H$  to the dynamic pressure  $q$  at the entrance to the section:

$$K = \frac{\Delta H}{q} = \frac{\Delta H}{\frac{1}{2}\rho V^2} \leftrightarrow \Delta H = K \cdot q \quad (1)$$

The loss coefficient of each section can be calculated using semi-empirical formulas, as explained above, according to Barlow et al. [40], where the different methods for each type of section are summarised.

An energy ratio was also calculated, which is the ratio of the jet power (the power in a flowing jet) in test section  $P_t$  to the rate of "flow losses" around the circuit, and is a measure of the efficiency of the wind tunnel. This ratio is usually reduced by 10% due to leaks and seals, and in case of a flow separation affecting the diffuser, it can be as low as 60%, so the power requirement could be doubled.

$$P_t = \frac{1}{2} \dot{m}_t V_t^2 = \frac{1}{2} \rho_t A_t V_t^3 \quad (2)$$

$$E_R = \frac{P_t}{\sum \Delta E} = \frac{P_t}{(\sum K) P_t} = \frac{1}{\sum K} \quad (3)$$

The energy ratio is used to compare the different design iterations and to compare the designed IWT with other wind tunnels (for an open-circuit tunnel, its value is usually between 3 and 7). It should be noted that this ratio is an indicator of the energy efficiency of the tunnel, not a measure of the value of the tunnel for research and development.

## 2.2. CFD Verification and Optimisation

CFD calculations have been used to verify the preliminary design, and also to study in detail the flow separation and boundary layer growth in some areas of the tunnel that were not sufficiently characterised with the methodology followed during the preliminary design phase. ANSYS CFX 2023R2 software [49], a general-purpose CFD software suite, has been used for this purpose.

The results obtained during this phase have feedback from the previous phase, and several iterations have been necessary to reach the final design, optimised according to the minimum pressure drop criterion, a value that can be calculated using this software.

In order to meet this criterion, it is essential that no local detachment of the boundary layer occurs.

Some of the areas, such as the air inlet of the IWT and the turning vanes in the corners, have been designed in detail during this phase, but with general empirical recommendations as a starting point [50–56]. These general recommendations do not go into a sufficient level of detail for design and manufacture, so it is necessary to use CFD tools or an experimental procedure to compare various solutions, where the CFD option is the most economical.

Since this type of software allows three-dimensional analysis and visual representations, it was also used to theoretically study the uniformity of the current in the test section core and to define the ideal conicity, to avoid the horizontal buoyancy phenomenon [40] (p. 78).

### 2.3. Building and Validation Tests

In this phase, the most important details of the building of the IWT designed in the previous phases are presented, and validation tests are carried out.

As one of the requirements is a low cost, it was decided that the construction of the IWT should be carried out by a company specialised in the production and installation of air-conditioning and ventilation ducts for buildings. To this end, the design has been adapted to the specifics and limitations of this type of company. Although some of the modifications to the original optimised design may involve a slight drop in aerodynamic efficiency, these concessions have a significant impact on the final cost, substantially reducing the building costs of the IWT.

When the construction of the IWT is completed, design validation tests will be performed, comparing the maximum value of the speed reached and the power consumed by the fan with the theoretical results of the design. In addition, the minimum temperature achievable by the installation during operation at maximum speed shall be measured. These validation tests are outside the scope of this article.

## 3. Preliminary Design

### 3.1. Requirements and Basic Configuration

In the design of this IWT, the dimensions and characteristics of the cold climate chamber in which it will be installed are the main design requirements. The chamber is 3.02 m wide, 3.78 m long and 4.66 m high. The effective width of the tunnel is limited to approximately 1 m, as the access door to the chamber is in the centre of one of the narrow walls.

The refrigerated chamber will determine the choice of the basic geometry of the IWT, which will be that of an open-circuit (non-return) tunnel with a closed test section. For the same test section size, the open-circuit configuration reduces the overall tunnel size and building costs.

Air intake and air discharge take place in the freezing chamber, which improves the temperature stability but requires the use of a closed test section, with a smaller test section core than in the case of an open test section. As there is no available space to make a linear wind tunnel, the diffuser has two corners (see Figure 3), to achieve a sufficient length to prevent flow separation. The diffuser is curved in a vertical direction instead of horizontally, leaving free space inside the chamber for operators and instrumentation, and making better use of the height of the chamber.

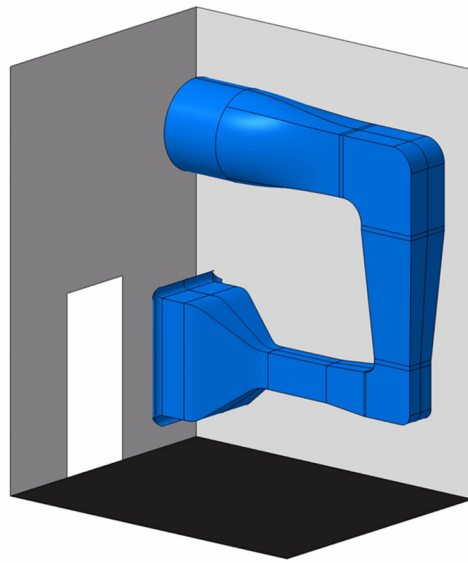


**Figure 3.** Designed IWT in the refrigerated chamber.

### 3.2. Objectives and Test Section

The objective of the IWT will be the testing of fixed-wing UAVs in icing conditions.

The first step in the design of any wind tunnel, after defining its purpose and basic configuration, is to define the dimensions of the test section and the speed to be reached [40] (p. 61). The test section will determine the dimensions of the remaining sections, the total size of the installation and, together with the speed, will also determine the required fan power.

The tunnel will be aimed at testing fixed-wing UAVs, and the 300 kg MTOW SIVA UAV has been used as a model for the design (see Figure 4). The SIVA is a medium-sized or Type II UAV according to the NATO classification, being in the 150 to 600 kg range, and is referred to as a tactical UAV [57]. It has a wingspan of 5.8 m, and its wing has an aerofoil, with a Reynolds number of  $2 \times 10^6$ , based on a wing chord of 0.9 m and a cruising speed of 40 m/s. The wing profile is an Eppler E580 airfoil, with a maximum chord thickness of 16.1%.



**Figure 4.** SIVA Unmanned Aerial Vehicle (UAV).

Defining a speed of 70 m/s in the test section, the Reynolds number per unit length is  $5.6 \times 10^6 \text{ m}^{-1}$  and the Mach is 0.2, which classifies it as a low-speed wind tunnel, as the compressibility phenomena are negligible (Mach below 0.3). This speed allows us to use aerofoils with a minimum of a 14 cm chord, to maintain a Reynolds number ( $Re$ ) of  $8 \times 10^5$  and thus ensure similar air behaviour with respect to the ratio between inertia and viscous

forces, and therefore the same boundary layer detachment and stall performance. Barlow et al. [40] (p. 64) recommend a minimum Reynolds number of between  $5 \times 10^5$  and  $8 \times 10^5$  based on wing chord for low-speed tunnels to be used for aeronautical development testing.

Another important factor to take into account is the blockage due to the tunnel walls, especially important in a closed test section. The blockage due to the presence of the model (solid blockage) and the wake blockage causes the effective velocity to increase around the model. This increases lift and drag, and this effective speed must be taken into account in the calculation of aerodynamic coefficients when the blockage ratio exceeds 5%. In any case, the ratio of the model “frontal area” to the test section total area should not exceed 10% [40] (p. 65). Lu et al. [58] also recommend not to exceed this 10% blockage limit. For tests with bluff bodies or with models that exceed this maximum recommended area, the blockage will be greater, so it will be necessary to perform prior CFD simulations to estimate its influence.

Defining a test section height of 0.4 m and a scale of 1:5 for a wing section of the SIVA UAV (and therefore a chord of 181 mm and a maximum thickness of 29.1 mm), the value for the blocked area is 7.3%, an acceptable value that represents an increase in effective speed of 0.42% (from 70.0 m/s to 70.3 m/s), calculated as the sum of the effect due to solid blockage [59] and the effect due to wake blockage [60]. In addition, a scale of 1:5 means a very convenient  $Re$  of  $8.9 \times 10^5$ . Smaller scales would reduce the Reynolds number and larger scales would increase the blockage (see Figure 5), so it is a good compromise point.

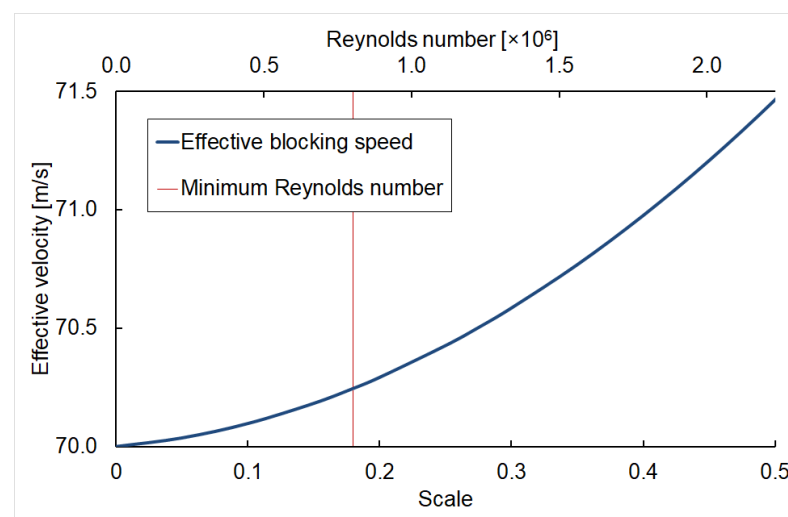


**Figure 5.** Effective blocking speed ( $v_{\text{uncorrected}} = 70$  m/s) and Reynolds number for different scales in the UAV SIVA wing.

Since the ratio between the width and height of the test section should not exceed a ratio of 2:3 [40] (p. 65), a test section height of 40 cm implies that the width of the test section will be 27 cm. Therefore, the tunnel will have a test area of  $0.1 \text{ m}^2$  ( $40 \times 27 \text{ cm}^2$ ) and will reach a speed of 70 m/s.

An optimum blockage of 5% for an accurate measurement of the aerodynamic coefficients will be obtained with profiles with a maximum thickness of 20 mm, which corresponds, for example, to a NACA 0012 airfoil with a chord of 167 mm. For models that are not aerofoils or do not occupy the full width, the optimum blockage of 5% corresponds to a frontal area of  $54 \text{ cm}^2$ .

### 3.3. IWT Sections

Some important aspects of the design of each of the sections of this open-circuit wind tunnel are discussed below. In all the calculations, the following environmental conditions have been assumed: a pressure of 94.15 kPa in a standard atmosphere, corresponding to the installation altitude of 615 m; a temperature of  $-20$  °C, reasonable for the intended



tests; and a resulting air density of 1.295 kg/m<sup>3</sup>. See Figure 6 for the nomenclature used for each section.

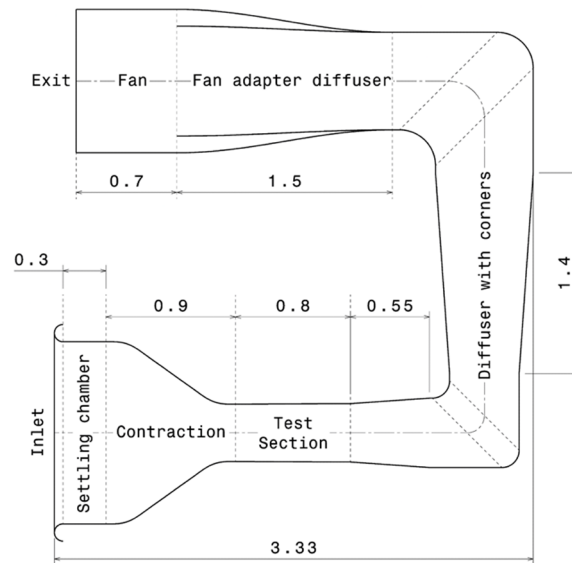


Figure 6. IWT sections.

### 3.3.1. Test Section

The test section is where the tests are carried out, and it is characterised by the highest tunnel speed and a uniform flow. It has a height of 40 cm and a width of 27 cm, giving an area of 0.108 m<sup>2</sup>. It has a length of 0.8 m, more than twice the hydraulic diameter, following a common recommendation in tunnel designs for this section.

The flow loss in a constant cross-section duct is given by the following formula, where  $f$  is the friction coefficient (Reynolds-dependent [61]) and  $\varnothing_h$  is the hydraulic diameter:

$$K_{Test\ Section} = f \frac{L}{\varnothing_h} \tag{4}$$

### 3.3.2. Settling Chamber

The settling chamber is the area responsible for uniformising the airflow prior to its acceleration in the contraction section or nozzle. It consists of an initial current-settling area, a honeycomb zone, a turbulence mesh screen and a final rear settling area, where the water-spraying instrumentation is installed. The length of this section is recommended to be a minimum of half of its hydraulic radius, so it has a total length of 0.30 m.

According to Prandtl [62] (p. 11), “a honeycomb is a guiding device through which the individual air filaments are rendered parallel”. It therefore serves as a flow straightener. The chosen honeycomb consists of hexagons with a size of 6.35 mm and a wall thickness of about 60 microns. Thus the honeycomb is composed of a total number of tubes in the order of 27,000, which is a value similar to that found in other tunnels (around 25,000 is a typical number [63]). The thickness for the honeycomb is 50 mm (it is recommended that the length of the tubes be between 6 and 8 times their hydraulic diameter).

The loss coefficient for the honeycomb can be calculated as follows [48], where  $\lambda$  is a parameter dependent on the material’s roughness, the hydraulic cell diameter and the Reynolds based on the honeycomb material’s roughness and the incoming flow speed, and  $\beta$  is the porosity.

$$K_{Honeycomb} = \lambda \left( \frac{L_{Honeycomb}}{\varnothing_{Honeycomb\ cell}} + 3 \right) \left( \frac{1}{\beta_{Honeycomb}} \right)^2 + \left( \frac{1}{\beta_{Honeycomb}} - 1 \right)^2 \tag{5}$$

The turbulence mesh screen is located behind the honeycomb. It has a porosity  $\beta$  of approximately 60% and serves to straighten the flow and improve the velocity distribution by achieving a spatially uniform steady stream of air in the test section.

The loss coefficient for a screen can be calculated as follows [40], where  $K_{Rn}$  is a parameter dependent on the Reynolds based on the wire diameter,  $K_{mesh}$  is the “mesh” factor (used to differentiate between smooth and rough wire) and  $\beta$  is the porosity.

$$K_{Rn} = 0.785 \left( \frac{Re_{wire}}{241} + 1 \right)^{-4} + 1.01 \quad (6)$$

$$K_{Mesh\ screen} = K_{mesh} K_{Rn} (1 - \beta_{Mesh\ screen}) + \frac{(1 - \beta_{Mesh\ screen})^2}{\beta_{Mesh\ screen}^2} \quad (7)$$

### 3.3.3. Contraction Section

The contraction section or nozzle is responsible for increasing the flow velocity through a contraction of the area entering the test section.

The contraction ratio of the IWT is 10 to 1, with the same ratio between height and width as in the test section, so the entrance is rectangular in shape, with a height of 1.27 m and a width of 0.85 m, an initial area of 1.08 m<sup>2</sup> and a total length of 0.90 m.

The flow loss can be approximated using that of a constant cross-section duct, but using the average friction coefficient between the inlet and outlet of the nozzle multiplied by a factor of 0.32, and using the hydraulic diameter at the beginning of the nozzle as the friction coefficient:

$$K_{Nozzle} = 0.32 \cdot f_{average} \frac{L}{\varnothing_h} \quad (8)$$

### 3.3.4. Diffuser and Corners

The diffuser is placed after the test section, and slows down the flow velocity with minimum pressure losses before the flow reaches the fan. By decreasing the velocity, the flow losses are reduced and the static pressure is restored for proper fan operation. In its final section, the diffuser also converts the rectangular section of the tunnel to the circular section of the fan.

The diffuser is very sensitive to design errors that can lead to the detachment of the current [64], increasing the flow losses of the entire tunnel and even causing vibrations affecting the fan or the stability of the speed in the test section [65]. Since it is also one of the sections with the highest pressure loss in the entire circuit, its design is particularly critical for the performance of the tunnel.

The main limitation is the length of the refrigerated chamber, which prevents the use of an ideal diffuser, which would be one without corners, with a cone angle of 3°, a minimum length of 2.4 m (3 to 4 times the length of the test section is recommended) and an area ratio of 1 to 2–3 between the start and end [40] (p. 81).

As it is not possible to use a straight diffuser, it is necessary to incorporate corners, and the diffuser has the following subsections: first diffuser (horizontal), first corner, second diffuser (vertical ascending), second corner and third diffuser (horizontal, which adapts the rectangular section to the circular section of the fan).

The first two sections of the diffuser are rectangular in cross-section, so although the angle of each face to the centre line is 4°, the angle of the equivalent cone is greater, in this case around 4.5°. The equivalent conicity of the third fan adapter diffuser is 6.0°.

The final full diffuser, after the iterative process described below, has a final to initial area ratio of 7.15 and an equivalent length of 5.16 m, with an overall conicity of 3.5°, due to the equivalent length of the corners, where there is no increase in the section.

Expanding corners are sometime used [66–69], but they add complexity in both design and manufacture, resulting in higher costs. In addition, they use higher-chord

turning vanes, which add frictional resistance and ultimately do not represent a substantial improvement.

### 3.3.5. Fan

The fan is responsible for moving the air through the tunnel circuit, compensating for pressure losses in the flow. The performance of the fan is higher the larger the diameter, so in the case of an open-circuit tunnel, it is usually installed just before the exit or before the settling chamber, but in the latter case, it is more difficult to achieve a quality flow in the test section.

In the selection of a motor, the most important parameters are the flow rate (defined by the test section and the maximum speed) and the pressure drop to be compensated for (estimated during the design). The selection of the fan is an iterative process, since the diameter of the fan changes the diffuser and therefore the pressure drop in the tunnel.

The power in a flowing jet is calculated as the dynamic pressure in the test section multiplied by the flow rate, and for this tunnel, it is 24 kW.

$$P_t = \frac{1}{2} \dot{m}_t V_t^2 = \frac{1}{2} \rho_t A_t V_t^3 \quad (9)$$

But this formula is for jet flows that release air directly to the outside, without a diffuser. In the case of a wind tunnel with a diffuser, the power to be delivered by the fan (excluding motor and fan losses) is lower, and can be estimated by the energy ratio.

$$E_R = \frac{P_t}{P_c} \leftrightarrow P_c = \frac{P_t}{E_R} \quad (10)$$

In this case, the energy ratio is 4.74, already decreased by 10% to be conservative. The efficiency of the selected fan is 0.66 for the flow rate and estimated pressure drop.

Therefore, the electrical power required to move the flow of air through the tunnel is 7.7 kW. It should be noted that in IWTs, it is common for the cooling power to ultimately determine the maximum speed, as the cost for tunnel cooling is about 10 to 20 times more expensive than for the tunnel drive [70].

### 3.3.6. Exit

As an open-circuit tunnel, the air exit also involves a pressure loss, due to the loss of the kinetic energy of the air as it is expelled into the chamber.

This flow loss is equal to a constant  $K_{exit}$  for the dynamic pressure at the exit. The constant corresponds to the formula

$$K_{exit} = \frac{2 \left[ \left( 1 + \frac{\gamma-1}{2} M^2 \right)^{\frac{\gamma}{\gamma-1}} - 1 \right]}{\gamma M^2} \quad (11)$$

where  $\gamma$  is the specific heat ratio of air and  $M$  is the local Mach. For a low Mach,  $K_{exit}$  is almost equal to 1 (for  $M = 0.2$ ,  $K_{exit} = 1.01$ ). The diameter of the exit will be equal to the diameter of the fan and is fundamental, as it determines the velocity at the exit and therefore the dynamic pressure (which will be almost equal to the pressure loss).

Although a larger-diameter fan means less pressure loss at the exit (and better performance), it also requires a longer length for the diffuser (or a greater cone angle, which can lead to flow separation). In other words, as the diameter of the fan increases and the pressure loss at the exit decreases, the pressure loss in the diffuser increases due to its greater length, so a compromise solution must be found.

In response to this problem, a design with only one corner in the diffuser was tested during the initial design, so that the air exit was upwards. By reducing the number of corners, the pressure losses in the diffuser were reduced, but the fan had a smaller diameter, and the exit losses increased due to the higher speed. In the end, this design increased

the overall pressure loss by 10%, in addition to requiring a fan that could not be found commercially with the required power.

Adding the second corner increases the length of the diffuser and allows the use of a larger-diameter fan, improving the overall result and allowing the use of a commercial fan, which dramatically reduces costs.

The diameter of minimum pressure loss for the tunnel corresponds to 1.080 m (see Figure 7), and by using a commercial fan, the diameter closest to this value (that meets the other characteristics) was chosen.

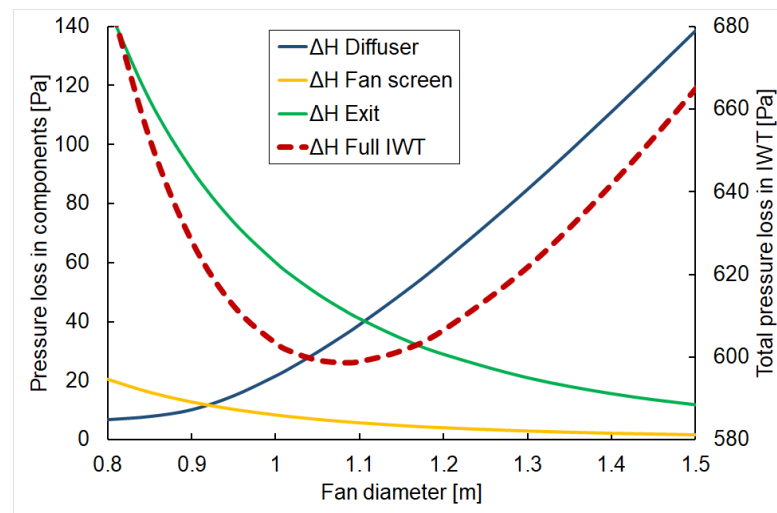


Figure 7. Pressure losses with fan diameter.

### 3.4. Comparison with Other Tunnels

The energy ratio achieved is quite high, especially for an open-circuit wind tunnel, which implies an efficient aerodynamic design. The semi-empirical method used was tested by Eckert et al. [48] and a comparative table of results is given in Table 1.

Table 1. Comparison of energy ratios in different wind tunnels.

Facility	Test Section Speed (m/s)	Current Energy Ratio (Best Available)	Computed Energy Ratio <sup>1</sup>	Difference (%)
NASA Ames, 40 × 80 ft	107.3	7.88	7.96	+1.0
NASA Ames, 7 × 10 ft	133.0	7.85	8.07	+2.8
Lockheed Martin low-speed wind tunnel	52.3	1.10	1.12	+1.8
Hawder Siddeley Aviation, 15-ft V/STOL	45.7	2.38	3.97	+66.8
University of Washington, 8 × 12 ft	117.7	8.30	7.20	−13.3
NASA Langley, 30 × 60 ft	52.7	3.71	4.73	+27.4
Indian Institute of Science <sup>2</sup> , 14 × 9 ft	96.3	6.85	6.83	−0.3
Wallisch et al. icing wind tunnel (IWT) <sup>2</sup>	35.0	—	3.01	—
INTA actual IWT <sup>2</sup>	70.0	4.16	4.36	+4.7
Designed IWT with no corners <sup>2</sup>	70.0	—	6.16	—
Designed IWT with one corner <sup>2</sup>	70.0	—	4.35	—
Designed and built IWT (with two corners) <sup>2</sup>	70.0	—	4.74	—

<sup>1</sup> In every IWT, a 10% reduction in the energy ratio has been applied. <sup>2</sup> Wind tunnel of the open-circuit type (non-return).

For the calculation of the energy ratio of the Wallisch et al. IWT [71], the measurements of some sections are not explicitly indicated, so they have been obtained through measurements in the figures given in the article.

It should be noted that the energy ratio of a tunnel is not as important as the quality of the flow in the test section or the capabilities of the measuring instruments (force

measurement system, laser anemometry systems [72], etc.). This ratio is only an indicator of aerodynamic efficiency, especially important in the case of an IWT due to cooling power limitations.

In the absence of space constraints, a straight IWT without corners (see Figure 8) and with similar characteristics would have a total length of 8.8 m, with a diffuser length of 6 m (for a taper of 3%). The pressure drop would be 464 Pa in that case, which would be 23% less than the IWT designed with two bends, and a 30% higher energy ratio.

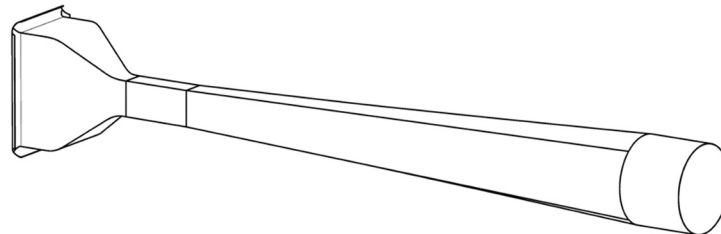


**Figure 8.** Straight IWT without corners.

### 3.5. Water Droplets and Ice Formation

As an icing wind tunnel, the spraying of water and its freezing are fundamental aspects to be taken into account in the design phase.

In-flight icing is caused by subcooled water droplets in suspension that freeze on impact with a surface, usually leading edges in the case of aircraft (the most critical areas for icing on fixed-wing aircraft are the wings and stabilisers). These droplets are mainly characterised by two parameters in addition to temperature: their size, characterised by their Median Volume Diameter (MVD), and their quantity, characterised by their Liquid Water Content (LWC). For individual droplets, their radius  $r_{drop}$  or their diameter  $d_{drop}$  can be used, as the MVD applies to sets of droplets with different sizes.

The usual system for spraying water consists of nozzles that spray water droplets of a controlled size and flow rate [70,71,73]. The water droplets are atomised at a temperature slightly above freezing to avoid ice blockage in the atomising nozzles, but these droplets must then be subcooled and accelerated to reach the desired test temperature and the appropriate velocity (that of the flow) at the moment of impact against the model. This defines a maximum droplet size to be used, beyond which the droplets will not reach the flow velocity or will not be at the same temperature as the flow when they reach the test section.

To calculate the droplet velocity, a time step procedure [71] based on the equation of movement can be used, disregarding gravity and assuming the droplets to be rigid spheres.

$$\Delta u_{drop} = \frac{1}{2} \rho_{air} \frac{\pi r_{drop}^2}{\frac{4}{3} \pi \rho_{water} r_{drop}^3} C_D (V - u_{drop})^2 \Delta t \quad (12)$$

For the calculation of the drag coefficient, a five-parameter empirical correlation can be used, proposed by Cheng [74] for a range of low Reynolds number values, which will be found in the contraction section.

$$C_D = \frac{24}{Re} (1 + 0.27 Re)^{0.43} + 0.47 \left[ 1 - \exp(-0.04 Re^{0.38}) \right] \quad (13)$$

This way, the velocity that different droplet sizes will reach when they advance through the circuit and are accelerated by the contraction section can be calculated. Setting a limiting velocity deviation of 3 m/s, the droplet size limit will be 65  $\mu\text{m}$  to reach a velocity of 67 m/s at the centre of the test section (1.6 m from the inlet).

To calculate the temperature [71] reached by the subcooled droplets, a time step procedure will be performed, similar to that of the velocity but, in this case, based on the first law of thermodynamics and disregarding evaporation, because a humidity close to

unity is considered. Heat transfer due to conduction depends on the Nusselt number for rigid spheres.

$$\Delta T_{drop} = \frac{3}{4} \frac{\dot{Q}_{conduction} + \dot{Q}_{radiation}}{\pi r_{drop}^3 \rho_{water} C_{v,water}} \Delta t \tag{14}$$

This way, the temperature that different droplet sizes will reach as they advance through the circuit and are accelerated by the current can be calculated (see Figure 9). Setting a temperature limit deviation of 0.5 °C for an IWT temperature of −3 °C, the droplet size limit will be 70 μm to reach a temperature of −2.5 °C at the centre of the test section (1.6 m from the inlet).

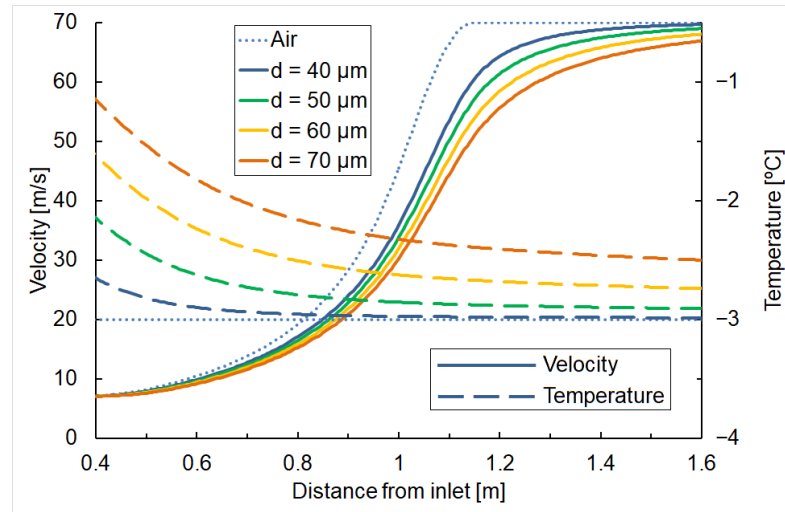


Figure 9. Development of velocity and temperature of droplets for different diameters.

On the other hand, when using scale models, it is necessary to scale other parameters in addition to velocity to achieve similarity with respect to ice formation [75], and one of these parameters to be scaled is the droplet size.

The inertia parameter *I* of Langmuir and Blodgett [76] is a dimensionless parameter that ensures that the trajectory of the droplets is the same in a real model and in the scale model, correctly simulating the impact of the droplets. To maintain this similarity, it will be necessary to adjust the droplet size according to the scale used. The modified inertia parameter *I*<sub>0</sub> is commonly used, the formula of which is

$$I_0 = \frac{1}{8} + \frac{\lambda}{\lambda_{Stokes}} \left( I - \frac{1}{8} \right), \text{ for } I = \frac{\rho_{water} \cdot d_{drop}^2 \cdot V}{18 \cdot r_{Leading\ Edge} \cdot \mu_{air}} > \frac{1}{8} \tag{15}$$

It should be noted that for *I* < 1/8, the droplets will follow the streamlines perfectly as they do not have enough inertia to be deflected, and therefore will not impact the model. This way, a limit can be obtained for the minimum droplet size that can be used in our scale model, which follows the formula below:

$$d_{drop} \geq \frac{3}{2} \sqrt{\frac{r_{Leading\ Edge} \cdot \mu_{air}}{\rho_{water} \cdot V}} \tag{16}$$

For a scale of 1:5 and the SIVA wing profile, at a speed of 70 m/s, droplets with a diameter of less than 1.0 μm will not impact (see Figure 10). This limit to the droplet size is especially important when using scale models, as it will usually be necessary to decrease the droplet size to maintain the similarity conditions, but without reaching this limit.

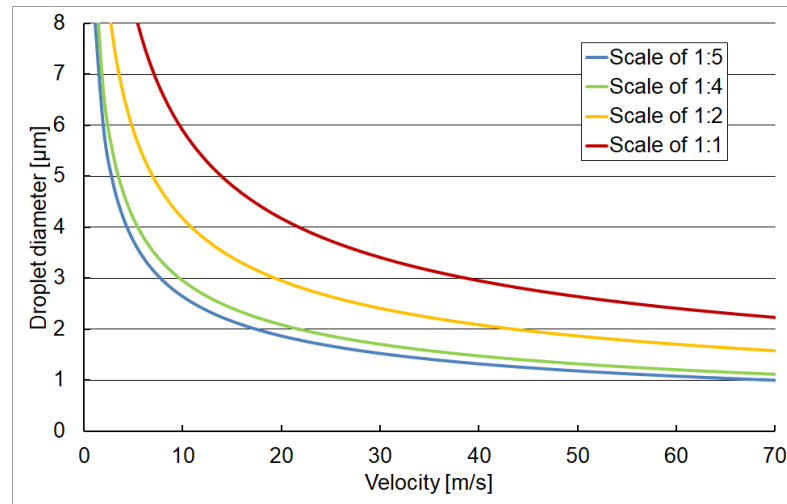


**Figure 10.** Minimum droplet diameter for impingement with different scales of SIVA wing aerofoil.

### 3.6. Estimated Cooling Power

The installed cooling power is 11.5 kW, and a temperature range of  $-25\text{ }^{\circ}\text{C}$  to  $+5\text{ }^{\circ}\text{C}$  is required, with a measurement instrumentation maximum uncertainty of  $\pm 0.5\text{ }^{\circ}\text{C}$  [77].

The cooling power of the chamber needs to compensate for heat losses through the walls of the chamber to maintain the temperature difference with the outside, but it must also compensate for the heat generated by the drive system, as well as the latent heat (released by the drops when they freeze) and the sensible heat (needed to cool the water drops to the chamber ambient temperature).

The sensible heat will be equal to the amount of water sprayed by the  $c_p$  of the water, times the temperature difference between the sprayed water and the ambient temperature; therefore

$$\dot{Q}_{sensible} = \dot{m}_{water} c_{p,water} \Delta T \quad (17)$$

The latent heat will be equal to the amount of water sprayed by the  $c_{latent}$  of the water; therefore

$$\dot{Q}_{latent} = \dot{m}_{water} c_{latent,water} \quad (18)$$

The amount of water per unit time (mass flow rate) will be equal to the flow rate in the tunnel per LWC, by the very definition of LWC (mass of water per volume of air).

$$\dot{m}_{water} = V_t A_t LWC \quad (19)$$

The power generated by the fan operation will be constant with the LWC, only depending on the speed to be reached in the test section.

According to these estimates (see Figure 11), a maximum LWC of  $1.2\text{ g/m}^3$  can be used for the maximum tunnel speed (70 m/s) and a chamber temperature of  $-20\text{ }^{\circ}\text{C}$ . The latent heat is significantly higher than the sensible heat. The maximum LWC can also be obtained for the installed cooling power, which will vary with the tunnel speed and the temperature to be reached (see Figure 12).

$$LWC_{max} = \frac{P_{cooling} - P_{fan}}{V_t A_t (\dot{Q}_{sensible} + \dot{Q}_{latent})} = \frac{P_{cooling} - \frac{1}{2} \rho_{air}(T) A_t V_t^3}{E_R \mu_{fan}}}{V_t A_t (c_{p,water} \Delta T + c_{latent,water})} \quad (20)$$

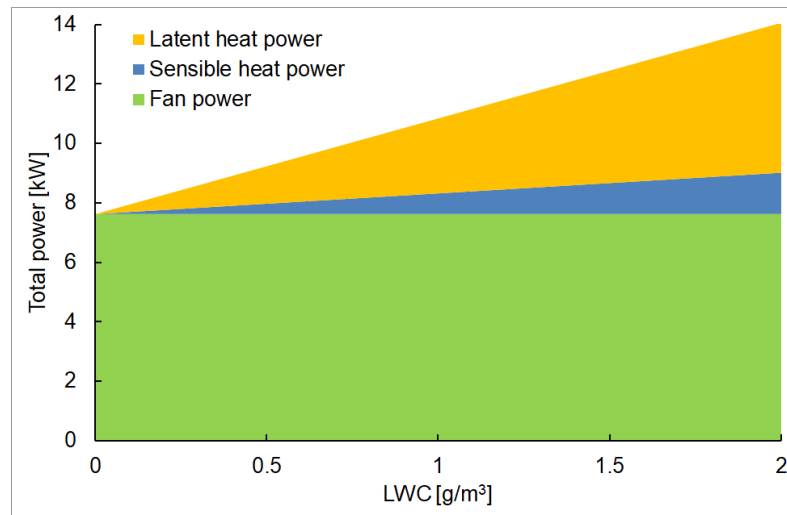


Figure 11. Cooling power required for  $\Delta T = -22\text{ }^\circ\text{C}$  and 70 m/s.

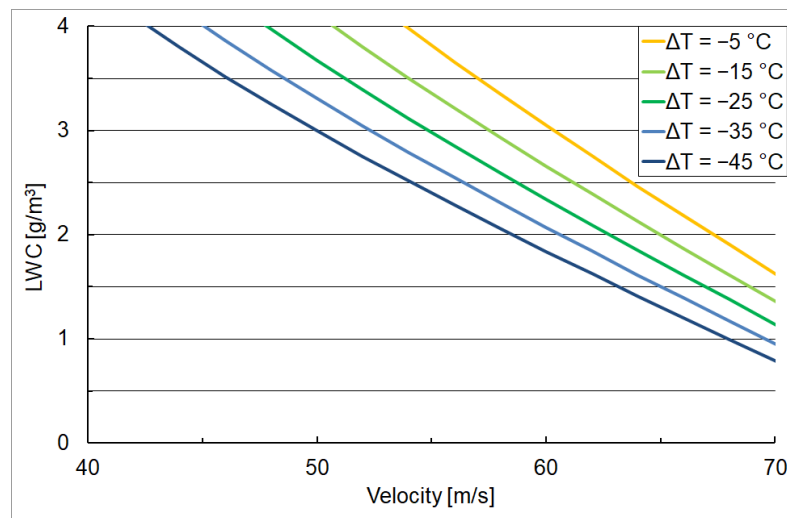


Figure 12. Maximum LWC with a cooling power of 11.5 kW.

#### 4. CFD Optimisation

The preliminary design of the wind tunnel was modelled according to the dimensions obtained, followed by several CFD simulations. Some sections have had to be modified because they showed flow separation, so the results presented here are the final ones, relating to the last iteration.

The model used takes advantage of the symmetry of the IWT, using  $6.6 \times 10^6$  elements and  $2.7 \times 10^6$  nodes for one of its halves. After performing several meshings according to general recommendations, it was found that finer meshes did not improve the results, requiring much more computational time, and that coarser meshes did not converge, so it was considered a good compromise solution. For the boundary layer, a triangular prism element inflation was used with a first element thickness of  $1 \times 10^{-5}$  m and a growth rate of 1.2 and it was 25 elements thick. In the rest of the duct, due to the meshing problems with cubic or prism elements in the corner sections and the diffuser with adaptation (from rectangular to circular cross-section), a tetragonal mesh was used with elements of 2 cm size, which was reduced to 1 cm in areas with higher gradients, such as the test section and corners.

The solver used was CFX, used by ANSYS, and a pressure-based solver, with an inlet turbulence of 1% to reflect the low turbulence of the flow after it passes through the honeycomb and the turbulence mesh screen. An “Outlet” type boundary was applied at



the exit, with the velocity corresponding to the flow rate of the circuit, thus replacing the fan. An “Opening” type boundary without relative pressure was applied at the inlet (see Figure 13). The turbulence was calculated with the high-resolution option.

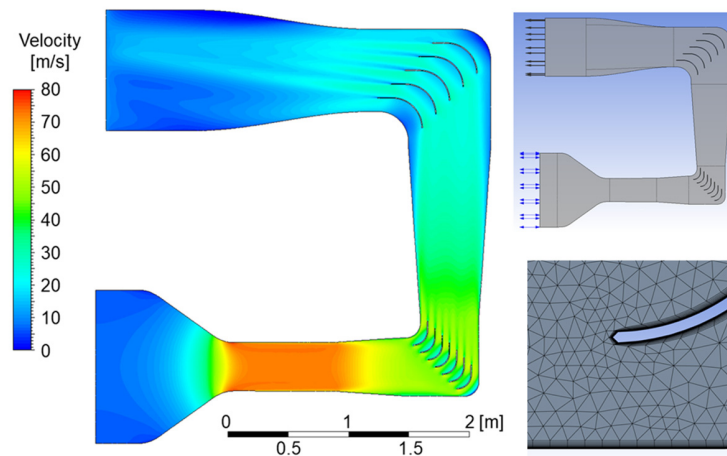


Figure 13. CFD simulation of the IWT with boundaries and inflation detail.

#### 4.1. General Verification

In the following table, the pressure drop in the different sections is compared, calculated analytically and by CFD. This serves to verify the theoretical results obtained by two different methods. The results can be seen in Table 2 numerically or in Figure 14 graphically.

Table 2. Pressure loss comparison between analytic model and CFD calculations.

Section	Analytical Pressure Drop		CFD Pressure Drop		Difference%
	Pa	%	Pa	%	
Settling chamber	0.1	0.0	0.1	0.0	—
Honeycomb	4.6	0.8	4.6 *	0.8	—
Mesh screen	25.9	4.3	25.9 *	4.3	—
Contraction	0.1	0.0	—	0.0	—
Test section	75.0	12.4	95.0	16.1	+26.6
Diffuser with corners	407.1	67.5	407.5	69.3	+0.1
Adaptation to fan diffuser	21.6	3.6	19.9	3.4	−8.1
Fan and mesh	9.0	1.5	9.1 *	0.1	+1.4
Exit	60.0	10.0	26.3	4.5	−56.2
Total	603.4	100.0	588.3	100.0	−2.5

\* This pressure drop was not calculated by CFD, so the value obtained by analytical calculations has been used instead.

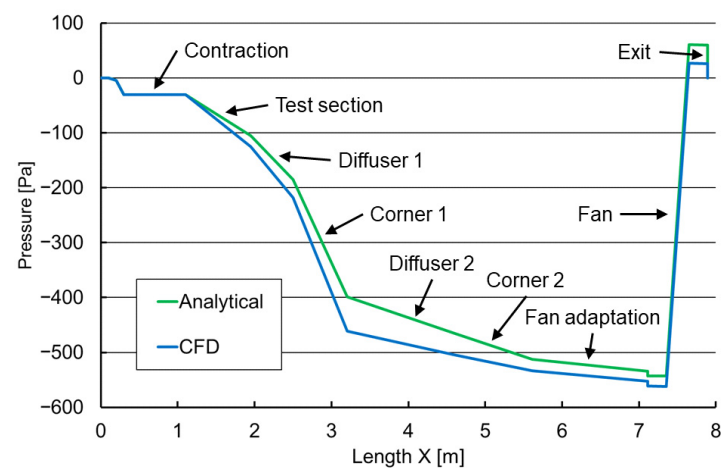


Figure 14. Drop of pressure along the IWT.

#### 4.2. Inlet Section

The inlet section is the area responsible for the air intake into the wind tunnel.

The clearance to the opposite wall (0.3 m) and the distance to the nearest side wall (0.3 m) are important to ensure the correct air entrance. These distances have been maximised, taking into account the size of the cold climate chamber where the tunnel is located and the limitations of the access door.

Although after the inlet section, the air is stabilised by honeycomb and a turbulence mesh screen, it is important that the inlet is as uniform as possible, so a rounding of the inlet edge as seen in Figure 15 has been incorporated, to avoid detachment of the boundary layer and turbulence at the edge of the inlet that can affect things downstream.

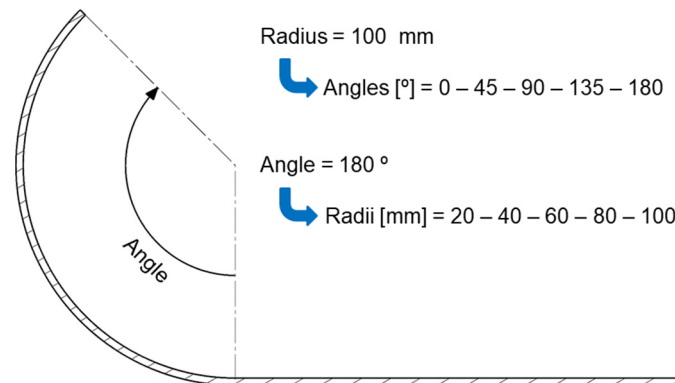


Figure 15. Rounded inlet.

The possible flow separation at this rounded inlet has been studied for several different angles of curvature, maintaining a constant radius of 100 mm. Figure 16 shows the velocity distribution for the cases of 0° (i.e., no rounding), 45°, 90°, 135° and 180°, respectively. As the angle increases, the flow in the settling chamber is more uniform as the flow separation decreases, especially in the case of 180°; so, it is decided to use this angle.

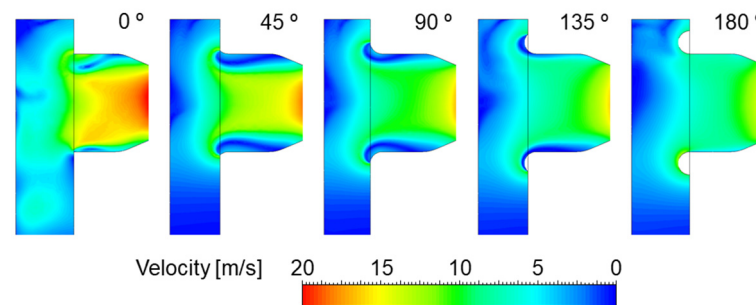
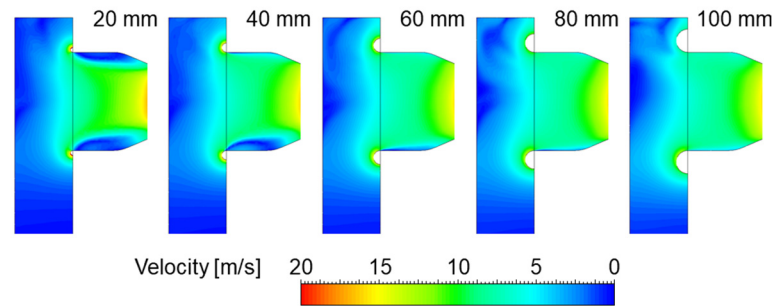


Figure 16. Air intake in the inlet section for different angles of a rounded inlet.

Next, the minimum radius that allows a uniform flow has been studied. The smallest possible radius that does not produce current detachment is desirable, in order to allow more free space on the side of the tunnel closest to the wall and a better air intake. The following radii have been studied for the entrance: 20, 40, 50, 60, 80 and 100 mm. Figure 17 shows the velocity distribution for the cases mentioned. It was decided to use 60 mm as the rounded inlet radius, as it has a minimum detachment that will eliminate the honeycomb and the mesh screen later.

Therefore an angle of 180° and a radius of 60 mm will be used for the inlet section.



**Figure 17.** Air intake in the inlet section for different radii of a rounded inlet.

#### 4.3. Contraction Section

It is essential that no flow separations occur in this section, so it has been modelled in more detail, and they have been found not to occur. The regions of adverse pressure gradient were checked to ensure that they were not too sharp, especially the curve at the exit of the contraction, just before the test section [78]. It can be verified that there are no detachments in the Section 4.4. Test Section, where the test section has been studied and it is observed that there are no flow separations due to the contraction section.

Although it was initially decided to use an AVA profile as in the Wallish et al. IWT [71], a profile consisting of constant curvature adaptations, which is comparatively much cheaper and simpler to manufacture, was finally used for production reasons, as seen in Figure 18.

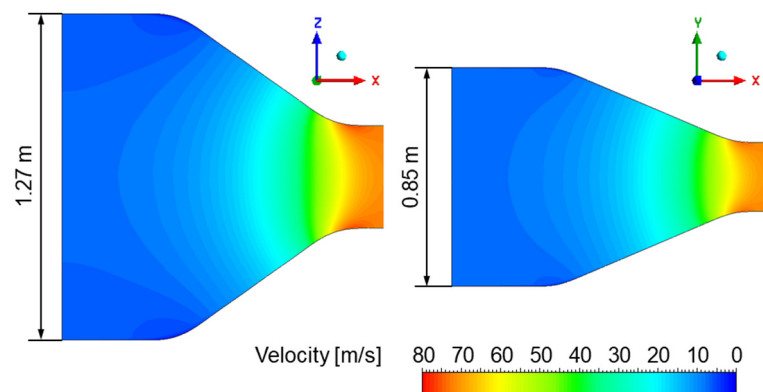


**Figure 18.** Contraction section or nozzle.

#### 4.4. Test Section

In the case of using parallel faces in the test section, the phenomenon of horizontal buoyancy will appear. As the thickness of the boundary layer increases along the length of a duct, the velocity in the rest of the section is accelerated to conserve the flow rate. This mainly affects the accuracy of the measurement of aerodynamic drag in the test section.

To avoid this effect that occurs in parallel-sided test sections, the area can be progressively increased, allowing the velocity in the centre of the duct to be kept constant. Different cone angles have been simulated using CFD, and a suitable cone angle of  $0.25^\circ$  on the top and bottom faces has been found that keeps the velocity constant. Both the top and bottom faces then form an angle of  $0.5^\circ$  to each other, keeping the side faces parallel. This means that the test section will have an initial height of 400 mm and a final height of 407 mm, while maintaining a constant width of 270 mm.

Figure 19 compares the velocities for the same test section, in one case with parallel faces and in the other with the described concity (each colour represents a velocity range of 0.1 m/s to magnify the velocity changes). It is observed that with the appropriate concity, the longitudinal component of the velocity remains stable throughout most of the test section.

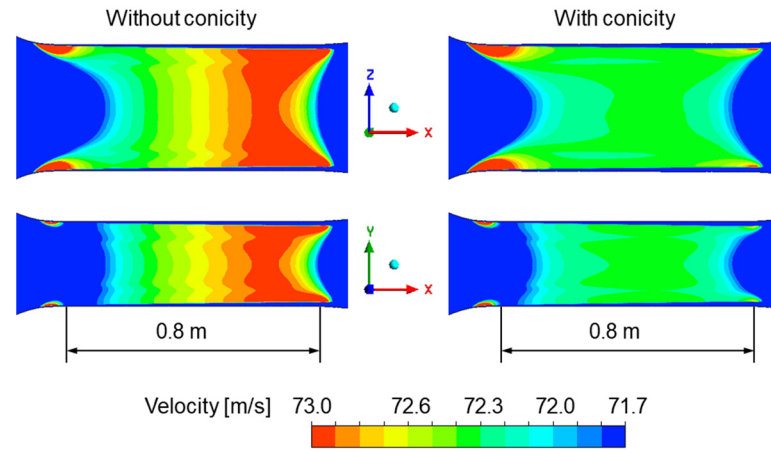


Figure 19. Horizontal buoyancy in the test section.

The quality of the current in the test section has also been studied, estimating the dimensions of the useful part of the flow, the test section core, which is the zone free from the effects of the boundary layer. The criterion used was that the velocity should not be higher or lower than 0.2 m/s of the average velocity at the centre of the section, which is 72.0 m/s. A deviation of 0.20–0.30% from the average velocity is a standard criterion in general-purpose wind tunnels [40]. It has been decided to use a more demanding criterion than the minimum for the IWT [77], which assumes a spatial uniformity of at least 2% for velocity (1.5 m/s) and angularity and 1% for static air temperature, obtained by experimental tests.

In addition to velocity uniformity, upflow (a critical flow angle for most aeronautical tests), cross-flow and unsteady flow are also important. The latter usually comes from the first diffuser, from the first corner or from air leaks, which generate flow separation, and which must be studied in the future by means of experimental tests.

The dimensions of the test section core are 400 mm (length) × 380 mm (height) × 248 mm (width). A settling length after the contraction of 200 mm is required to allow the velocity to become uniform. Remark that the boundary layer has a thickness of 11 mm at the central point of the test section, which means that the area of the test section core is about 87% of the total area. The velocity distribution of the test section can be seen in Figure 20.

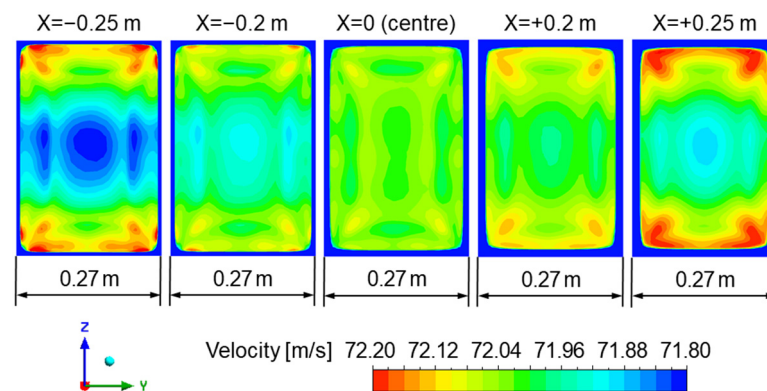


Figure 20. Flow quality in the test section.

## 5. Construction Details

### 5.1. Material and Structure

The material of choice was 2 mm thick galvanised steel sheet, so that it can withstand the corrosion due to the humid conditions of an IWT. The sheet metal has been formed and welded according to the specifications indicated, using the applicable standards [79,80] for the verification measurement. The thickness is sufficient to withstand the pressures that

appear in the different sections, and it is a very common thickness in this type of duct. The highest pressure appears in the test section, as it has a higher velocity. The air velocity of 70 m/s is equivalent to a dynamic pressure of 3174 Pa, i.e., 0.031 atm.

The circuit and the fan are attached to a structure firmly bolted to the floor and walls, with rubber pads on the supports to dampen possible vibrations, made of welded structural tube with a square cross-section of 70 mm. Stiffness is important to avoid vibrations. It includes the necessary accessories to compensate for the cyclical changes due to different temperatures and suffered by the structure, the tunnel itself and the fan.

The structure keeps the test section at a height of 1.2 m, which results in a comfortable working height for adjusting the models and instrumentation. The structure also serves as a support for the attachment of cameras for visualisation or for the installation of test instrumentation (see Figure 21).



**Figure 21.** IWT before painting.

Both the supporting structure and the wind tunnel sections are painted blue for increased corrosion protection. To avoid reflections when using laser anemometry systems, the test section has been painted matte black. This is also advantageous for flow visualisation tests.

### 5.2. Sections of the Wind Tunnel

All the sections are removable from each other and have stiffened ends by means of L-formed folds, which also allow them to be joined to each other by means of standard stainless steel screws. The joints between sections have a Teflon seal that ensures airtightness up to an ATC-5 level [81] and reduces pressure leaks (the maximum level of airtightness in ducts is ATC-6). The inside area has been taped, to ensure that there are no grooves or gaps that could cause flow separation, and there are no internal welds.

The test section is also removable, with a metal structure forming the edges and supporting the lateral, lower and upper flat faces. These faces are independently removable, and various types of walls can be mounted depending on the test to be performed: transparent methacrylate walls for flow visualisations, black or with painted patterns to improve the contrast of the background in visualisations, with supports for instrumentation or models, or with registers for quick access to the interior. Different types of walls can be combined on each side face, top or bottom, depending on the needs of the specific test.

As the air inlet is in a closed chamber and not outside, it is not necessary to install an anti-objects grille in the inlet. The settling chamber allows the extraction of two filter holder units using a register, where the aluminium honeycomb and the turbulence mesh

screen are mounted in the first one and the nozzles for spraying water in the second one. It is not possible to place the nozzles before the honeycomb or the mesh screen, as ice would accumulate on them. These removable filter holder units allow for quick changes in case of damage, for maintenance or for mounting different configurations of spraying devices depending on the needs of each test. The mesh screen often accumulates dust, so easy removal for cleaning is operationally important. The nozzles and heated pressurised water pipes are mounted on crossbars, fused with aerofoil-shaped 3D-printed parts to minimise the turbulence that can reach the test section. Distilled water from a pre-filled tank is used, and the measure of heating the tubes is a simple and effective way to prevent freezing in the nozzles, without using chemicals that could change the icing behaviour of the water.

At the lowest point of the tunnel, in the diffuser, a register has been incorporated to remove the liquid water generated after the thawing of the ice formed during the tests, and there are also cleanouts before and after each corner for the quick manual de-icing of the turning vanes, in case it is necessary to avoid long tunnel downtimes during the test campaigns. These cleanouts can be clearly seen in Figure 22.



**Figure 22.** Final IWT in the cold climate chamber.

Turning vanes are bent sheets with a constant curvature and a straight exit area, welded on the inside and following general tunnel design recommendations [50–56]. This design minimises the cost of construction, as it is not fused.

### 5.3. Fan Selection

The section housing the fan supports the largest structural loads and must be able to support the motor in its critical case (loss of half of the blades on one side). The drive system weighs around 240 kg and is mounted on dampers to avoid transmitting vibrations to the rest of the tunnel.

For the wind tunnel size, axial fans are used, thanks to their higher efficiency. A commercial fan has been selected, rather than one designed and built specifically for this IWT, resulting in a significant cost reduction at the expense of a slight loss in efficiency.

The fan selected is a tubular helical fan with a diameter of 1000 mm, with galvanised corrosion protection on the casing and 9 aluminium aerofoil blades with steel drive bushings. The motor uses a three-phase power supply at 400 V and 50 Hz, consists of four poles and has IP55 protection (protected against dust ingress and resistant to water jets from any direction) [82]. It has an operating point fan efficiency of 66% and a maximum shaft power of 11 kW.

The fan is fitted with a safety mesh screen to prevent damage to the blades due to possible impacts from flying ice. However, the blade tips could be damaged if small pieces of ice were to pass through the mesh screen and interfere with the clearance between the blade tips and the walls. For this reason, the blades can be easily replaced in case of damage.

## 6. Conclusions

An iterative design process based on well-proven semi-empirical formulas and supported by CFD calculations has been shown to be a very good approach for the design and aerodynamic optimisation of a low-cost IWT.

The IWT designed is an open-circuit type (non-return), with two corners, overall dimensions of 3.3 m (length)  $\times$  1 m (width)  $\times$  3.6 m (height) and a test section size of 0.40 m  $\times$  0.27 m, and it allows a velocity up to 70 m/s. The maximum Reynolds is  $5.6 \times 10^6 \text{ m}^{-1}$ . It requires a fan power of 7.7 kW and achieves an energy ratio of 4.74. With the installed cooling capacity of 11.5 kW, a maximum LWC of  $1.2 \text{ g/m}^3$  (for maximum tunnel speed) can be achieved. It allows the use of droplets with a maximum diameter of 65  $\mu\text{m}$  and a minimum diameter that depends on the scale of the model to be tested, but will be in the range of 1–2  $\mu\text{m}$ .

The restriction of an existing cold climate chamber (without a longitudinal dimension larger than the other dimensions) makes it necessary to introduce corners, despite the use of an open-circuit wind tunnel, but this has not resulted in an excessive loss of aerodynamic efficiency.

Being manufactured by a company specialising in air conditioning duct manufacturing and building ventilation installation, as well as a modular design aimed at easy fabrication, together with the selection of materials common in the industry and the adaptation to a commercial fan, greatly reduce the manufacturing costs of the IWT.

Once the construction of the IWT has been completed, validation tests will be carried out, comparing the results with the theoretical values of the design. These validation tests, as well as subsequent improvements to the IWT, will be the subject of a future article.

Therefore, this paper demonstrates that it is feasible to design and build a cost-effective IWT for testing small to medium-sized fixed-wing UAVs, enabling the research and development of ice protection systems needed to expand the use and capabilities of this type of aircraft, describing in detail the design process and highlighting the main features that need to be considered, not only for a general-purpose wind tunnel but specifically for an IWT for UAV testing.

**Author Contributions:** Conceptualisation, J.C.P.d.P. and F.T.R.; methodology, J.C.P.d.P.; validation, J.C.P.d.P. and J.M.N.; formal analysis, J.C.P.d.P.; investigation, J.C.P.d.P.; resources, J.C.P.d.P. and J.M.N.; writing—original draft preparation, J.C.P.d.P.; writing—introduction, J.M.N. and A.G.-M.; writing—review and editing, J.C.P.d.P., J.M.N., A.G.-M., F.T.R. and R.A.P.; visualisation, J.C.P.d.P.; funding acquisition, F.T.R. and R.A.P. All authors have read and agreed to the published version of the manuscript.

**Funding:** The article-processing charges (APCs) were funded by Fundación Universidad Alfonso X el Sabio (FUAX).

**Institutional Review Board Statement:** Not applicable.

**Informed Consent Statement:** Not applicable.

**Data Availability Statement:** Data is contained within the article.

**Acknowledgments:** We would like to thank Paloma García and Francisco Carreño for the IWT construction information and photographs provided, as well as Rebeca Martínez for editing the IWT photographs.

**Conflicts of Interest:** The authors declare no conflicts of interest.

## References

- Martini, F.; Contreras Montoya, L.T.; Ilinca, A. Review of wind turbine icing modelling approaches. *Energies* **2021**, *14*, 5207. [[CrossRef](#)]
- Gerrie, S.; Islam, S.Z.; Gerrie, C.; Droubi, G.; Asim, T. The Impact of Ice Formation on Vertical Axis Wind Turbine Performance and Aerodynamics. *Wind* **2023**, *3*, 16–34. [[CrossRef](#)]
- Zhang, Z.; Zhang, H.; Yue, S.; Zeng, W. A review of icing and anti-icing technology for transmission lines. *Energies* **2023**, *16*, 601. [[CrossRef](#)]
- Li, B.; Bai, J.; He, J.; Ding, C.; Dai, X.; Ci, W.; Zhu, T.; Liao, R.; Yuan, Y. A review on superhydrophobic surface with anti-icing properties in overhead transmission lines. *Coatings* **2023**, *13*, 301. [[CrossRef](#)]
- Zhou, L.; Liu, R.; Yi, X. Research and development of anti-icing/deicing techniques for vessels. *Ocean Engineering* **2022**, *260*, 112008. [[CrossRef](#)]
- Cao, Y.; Tan, W.; Wu, Z. Aircraft icing: An ongoing threat to aviation safety. *Aerosp. Sci. Technol.* **2018**, *75*, 353–385. [[CrossRef](#)]
- Gultepe, I. A review on weather impact on aviation operations: Visibility, wind, precipitation, icing. *J. Airl. Oper. Aviat. Manag.* **2023**, *2*, 1–44. [[CrossRef](#)]
- Jarošová, M.; Janošková, A. Meteorological causes of air accidents. *Transp. Res. Procedia* **2023**, *75*, 183–188. [[CrossRef](#)]
- Bromfield, M.A.; Horri, N.; Halvorsen, K.; Lande, K. Loss of control in flight accident case study: Icing-related tailplane stall. *Aeronaut. J.* **2023**, *127*, 1554–1573. [[CrossRef](#)]
- Zhao, Y.; Guo, Q.; Lin, T.; Cheng, P. A review of recent literature on icing phenomena: Transport mechanisms, their modulations and controls. *International. J. Heat Mass Transf.* **2020**, *159*, 120074. [[CrossRef](#)]
- Yamazaki, M.; Jemcov, A.; Sakaue, H. A review on the current status of icing physics and mitigation in aviation. *Aerospace* **2021**, *8*, 188. [[CrossRef](#)]
- Zeng, D.; Li, Y.; Liu, H.; Yang, Y.; Peng, L.; Zhu, C.; Zhao, N. Superhydrophobic coating induced anti-icing and deicing characteristics of an airfoil. *Colloids Surf. A Physicochem. Eng. Asp.* **2023**, *660*, 130824. [[CrossRef](#)]
- Mousavi, S.M.; Sotoudeh, F.; Chun, B.; Lee, B.J.; Karimi, N.; Faroughi, S.A. The potential for anti-icing wing and aircraft applications of mixed-wettability surfaces—A comprehensive review. *Cold Reg. Sci. Technol.* **2023**, *217*, 104042. [[CrossRef](#)]
- Long, C.; Jinghang, X.; Xichun, L.; Zhanqiang, L.; Bing, W.; Qinghua, S.; Yukui, C.; Yi, W.; Xiangyu, G.; Chunlong, L. Micro/nano manufacturing aircraft surface with anti-icing and deicing performances: An overview. *Nanotechnol. Rev.* **2023**, *12*, 20230105. [[CrossRef](#)]
- Liu, Z.; Gao, Z.; Wu, H.; Yan, L.; Mei, Y.; Peng, H.; Wang, H.; Du, J.; Zheng, B.; Guo, Y. Phase-transition-induced phosphorescence: A novel icing detection strategy for airplane. *Dye. Pigment.* **2024**, *223*, 111969. [[CrossRef](#)]
- He, Q.; Li, K.; Xu, Z.; Wang, J.; Wang, X.; Li, A. Research progress on construction strategy and technical evaluation of aircraft icing accretion protection system. *Chin. J. Aeronaut.* **2023**, *36*, 1–23. [[CrossRef](#)]
- He, Z.; Xie, H.; Jamil, M.I.; Li, T.; Zhang, Q. Electro-/Photo-Thermal Promoted Anti-Icing Materials: A New Strategy Combined with Passive Anti-Icing and Active De-Icing. *Adv. Mater. Interfaces* **2022**, *9*, 2200275. [[CrossRef](#)]
- Yu, B.; Sun, Z.; Liu, Y.; Wu, Y.; Zhou, F. Photo-thermal superhydrophobic sponge for highly efficient anti-icing and de-icing. *Langmuir* **2023**, *39*, 1686–1693. [[CrossRef](#)]
- Xie, Z.; Tian, Y.; Shao, Y.; Wang, H.; Chen, R.; Zhu, X.; Liao, Q. Recent progress in anti-icing and deicing applications of the photothermal conversion materials. *Prog. Org. Coat.* **2023**, *184*, 107834. [[CrossRef](#)]
- Wu, Y.; Dong, L.; Shu, X.; Yang, Y.; Feng, P.; Ran, Q. Recent advancements in photothermal anti-icing/deicing materials. *Chem. Eng. J.* **2023**, *469*, 143924. [[CrossRef](#)]
- Piscitelli, F.; Palazzo, S.; De Nicola, F. Icing Wind Tunnel Test Campaign on a Nacelle Lip-Skin to Assess the Effect of a Superhydrophobic Coating on Ice Accretion. *Appl. Sci.* **2023**, *13*, 5183. [[CrossRef](#)]
- Piscitelli, F. Characterization in Relevant Icing Conditions of Two Superhydrophobic Coatings. *Appl. Sci.* **2022**, *12*, 3705. [[CrossRef](#)]
- Yu, L.; Wu, Y.; Zhao, H.; Zhu, D. A Study on the Sensitivities of an Ice Protection System Combining Thermoelectric and Superhydrophobic Coating to Icing Environment Parameters. *Appl. Sci.* **2023**, *13*, 6607. [[CrossRef](#)]
- Villeneuve, E.; Ghinet, S.; Volat, C. Experimental Study of a Piezoelectric De-Icing System Implemented to Rotorcraft Blades. *Appl. Sci.* **2021**, *11*, 9869. [[CrossRef](#)]
- Liu, Y.; Wang, Q.; Yi, X.; Chen, N.; Ren, J.; Li, W. An anti-icing scaling method for wind tunnel tests of aircraft thermal ice protection system. *Chin. J. Aeronaut.* **2024**, *37*, 1–6. [[CrossRef](#)]
- Hann, R.; Enache, A.; Nielsen, M.C.; Stovner, B.N.; van Beeck, J.; Johansen, T.A.; Borup, K.T. Experimental Heat Loads for Electrothermal Anti-Icing and De-Icing on UAVs. *Aerospace* **2021**, *8*, 83. [[CrossRef](#)]
- Hann, R.; Johansen, T.A. *Unsettled Topics in Unmanned Aerial Vehicle Icing*; SAE Technical Paper EPR2020008; Norwegian University of Science and Technology: Warrendale, PA, USA, 2020. [[CrossRef](#)]
- Jiménez-Jiménez, S.I.; Ojeda-Bustamante, W.; Marcial-Pablo, M.D.J.; Enciso, J. Digital terrain models generated with low-cost UAV photogrammetry: Methodology and accuracy. *ISPRS Int. J. Geo-Inf.* **2021**, *10*, 285. [[CrossRef](#)]
- Hu, T.; Sun, X.; Su, Y.; Guan, H.; Sun, Q.; Kelly, M.; Guo, Q. Development and performance evaluation of a very low-cost UAV-LiDAR system for forestry applications. *Remote Sens.* **2020**, *13*, 77. [[CrossRef](#)]
- Granados-Bolaños, S.; Quesada-Román, A.; Alvarado, G.E. Low-cost UAV applications in dynamic tropical volcanic landforms. *J. Volcanol. Geotherm. Res.* **2021**, *410*, 107143. [[CrossRef](#)]



31. Famiglietti, N.A.; Cecere, G.; Grasso, C.; Memmolo, A.; Vicari, A. A test on the potential of a low cost unmanned aerial vehicle RTK/PPK solution for precision positioning. *Sensors* **2021**, *21*, 3882. [CrossRef]
32. Lussem, U.; Schellberg, J.; Bareth, G. Monitoring forage mass with low-cost UAV data: Case study at the Rengen grassland experiment. *PFG–J. Photogramm. Remote Sens. Geoinf. Sci.* **2020**, *88*, 407–422. [CrossRef]
33. Schaefer, M.; Teeuw, R.; Day, S.; Zekkos, D.; Weber, P.; Meredith, T.; Van Westen, C.J. Low-cost UAV surveys of hurricane damage in Dominica: Automated processing with co-registration of pre-hurricane imagery for change analysis. *Nat. Hazards* **2020**, *101*, 755–784. [CrossRef]
34. Liu, S.; Yang, X.; Zhou, X. Development of a low-cost UAV-based system for CH<sub>4</sub> monitoring over oil fields. *Environ. Technol.* **2021**, *42*, 3154–3163. [CrossRef] [PubMed]
35. EASA Certification Specifications and Acceptable Means of Compliance for Large Aeroplanes (CS-25). European Union Aviation Safety Agency (EASA) Amendment 28, 15 December 2023. Available online: <https://www.easa.europa.eu/en/document-library/certification-specifications/group/cs-25-large-aeroplanes> (accessed on 16 June 2024).
36. STANAG 4671; Fixed-Wing Unmanned Aircraft Systems Airworthiness Requirements (USAR)—AEP-4671 Edition B. United States Department of Defense, NATO Standardization Agency (NSA): Washington, DC, USA, 2022. Available online: <https://publishers.standardstech.com/content/military-dod-stanag-4671> (accessed on 16 June 2024).
37. STANAG 4702; Rotary Wing Unmanned Aircraft Systems Airworthiness Requirements (USAR)—AEP-80 Edition B. United States Department of Defense, NATO Standardization Agency (NSA): Washington, DC, USA, 2022. Available online: <https://publishers.standardstech.com/content/military-dod-stanag-4702> (accessed on 16 June 2024).
38. STANAG 4703; Light Unmanned Aircraft Systems Airworthiness Requirements (USAR)—AEP-83 Edition B. United States Department of Defense, NATO Standardization Agency (NSA): Washington, DC, USA, 2022. Available online: <https://publishers.standardstech.com/content/military-dod-stanag-4703> (accessed on 16 June 2024).
39. Renau Martínez, J.; García Peñas, V.; Ibáñez Arnal, M.; Giménez Sancho, A.; López González, E.; García Magariño, A.; Terroba Ramírez, F.; Moreno Ayerbe, F.J.; Sánchez López, F. Design Process and Advanced Manufacturing of an Aquatic Surface Vehicle Hull for the Integration of a Hydrogen Power Plant Propulsion System. *J. Mar. Sci. Eng.* **2024**, *12*, 268. [CrossRef]
40. Barlow, J.B.; Rae, W.H.; Pope, A. *Low-Speed Wind Tunnel Testing*, 3rd ed.; John Wiley & Sons: New York, NY, USA, 1999; ISBN 978-0-471-55774-6.
41. Cattafesta, L.; Bahr, C.; Mathew, J. Fundamentals of Wind-Tunnel Design. In *Encyclopedia of Aerospace Engineering*, 1st ed.; John Wiley & Sons: New York, NY, USA, 2010. [CrossRef]
42. Quinn, D.B.; Watts, A.; Nagle, T.; Lentink, D. A new low-turbulence wind tunnel for animal and small vehicle flight experiments. *R. Soc. Open Sci.* **2017**, *4*, 160960. [CrossRef] [PubMed]
43. Szwaba, R.; Hinc, K.; Ochrymiuk, T.; Krzemianowski, Z.; Doerffer, P.; Kurowski, M. Open low speed wind tunnel—Design and testing. *Arch. Thermodyn.* **2021**, *42*, 57–70. [CrossRef]
44. Almeida, O.; Miranda, F.C.; Ferreira Neto, O.; Saad, F.G. Low Subsonic Wind Tunnel—Design and Construction. *J. Aerosp. Technol. Manag.* **2018**, *10*, e1018. [CrossRef]
45. Pezzotti, S.; D’Iorio, J.I.; Nadal-Mora, V.; Pesarini, A. A wind tunnel for anemometer calibration in the range of 0.2–1.25 m/s. *Flow Meas. Instrum.* **2011**, *22*, 338–342. [CrossRef]
46. Farnsworth, J.; Sinner, D.; Gloutak, D.; Droste, L.; Bateman, D. Design and qualification of an unsteady low-speed wind tunnel with an upstream louver system. *Exp. Fluids* **2020**, *61*, 181. [CrossRef]
47. Azzawi, I.D.J. Design and characterizing of blower wind tunnel using experimental and numerical simulation. *Proc. Inst. Mech. Eng. Part G J. Aerosp. Eng.* **2023**, *237*, 3582–3596. [CrossRef]
48. Eckert, W.T.; Mort, K.W.; Jope, J. *Aerodynamic Design Guidelines and Computer Program for Estimation of Subsonic Wind Tunnel Performance*; NASA Technical Note TN D-8243; National Aeronautics and Space Administration: Washington, DC, USA, 1976.
49. Ansys Fluent Fluid Simulation Software. ANSYS, Inc. Available online: <https://www.ansys.com/products/fluids/ansys-fluent> (accessed on 30 June 2024).
50. Kröber, G. *Guide Vanes for Deflecting Fluid Currents with Small Loss of Energy*; National Advisory Committee for Aeronautics (NACA) Technical Memorandum 722; National Advisory Committee for Aeronautics: Washington, DC, USA, 1933. Available online: <https://ntrs.nasa.gov/citations/19930094695> (accessed on 16 June 2024).
51. Collar, A.R. *Some Experiments with Cascades of Airfoils*; Aeronautical Research Council Reports and Memoranda 1768; National Physical Laboratory: London, UK, 1936.
52. Johl, G.; Passmore, M.; Render, P. Design and performance of thin, circular arc, wind-tunnel turning vanes. *Aeronaut. J.* **2007**, *111*, 115–118. [CrossRef]
53. Winter, K.G. Comparative Tests of Thin Turning Vanes in the RAE 4 × 3 Foot Wind Tunnel. Aeronautical Research Council Reports and Memoranda 2589. 1947. Available online: <https://reports.aerade.cranfield.ac.uk/handle/1826.2/3044> (accessed on 16 June 2024).
54. Sahlin, A.; Johansson, A.V. Design of guide vanes for minimizing the pressure loss in sharp bends. *Phys. Fluids A Fluid Dyn.* **1991**, *3*, 1934–1940. [CrossRef]
55. Gelder, T.F.; Moore, R.D.; Sanz, J.M.; McFarland, E.R. Wind Tunnel Turning Vanes of Modern Design. AIAA 1986-44. In Proceedings of the 24th Aerospace Sciences Meeting, Reno, NV, USA, 6–9 January 1986. [CrossRef]

56. Patterson, G.N. *Note on the Design of Corners in Duct Systems*; Aeronautical Research Council Reports and Memoranda 1773; H.M. Stationery Office: London, UK, 1937.
57. Mayer, J.E. *State of the Art of Airworthiness Certification*; NATO STO-MP-AVT-273; NATO Science & Technology Organization (STO): Laurel, MD, USA, 2017.
58. Lu, D.; Lu, Z.; Han, Z.; Xu, X.; Huang, Y. Numerical Investigation on the Effect of Blockage on the Icing of Airfoils. *Aerospace* **2022**, *9*, 587. [[CrossRef](#)]
59. Glauert, H. *Wind Tunnel Interference on Wings, Bodies and Airscrews*; British Aeronautical Research Council, Reports & Memoranda, No. 1566; H.M. Stationery Office: London, UK, 1933.
60. Maskell, E.C. *A theory of the Blockage Effects on Bluff Bodies and Stalled Wings in a Closed Wind Tunnel*; British Aeronautical Research Council, Reports & Memoranda, No. 3400; H.M. Stationery Office: London, UK, 1963.
61. Shames, I.H. Chapter 9. In *Mechanics of Fluids*, 3rd ed.; McGraw-Hill: New York, NY, USA, 1992.
62. Prandtl, L. *Attaining a Steady Air Stream in Wind Tunnels*; National Advisory Committee for Aeronautics (NACA) Technical Memorandum 726; National Advisory Committee for Aeronautics: Washington, DC, USA, 1933. Available online: <https://ntrs.nasa.gov/citations/1993009469> (accessed on 16 June 2024).
63. Mehta, R.D.; Bradshaw, P. Design rules for small low speed wind tunnels. *Aeronaut. J.* **1979**, *83*, 443–453. [[CrossRef](#)]
64. Robertson, J.M.; Fraser, H.R. Separation Prediction for Conical Diffusers. *ASME J. Basic Eng.* **1960**, *82*, 201–209. [[CrossRef](#)]
65. Abdel Aziz, S.S.; Moustafa, E.B.; Salem Said, A.-H.S. Experimental Investigation of the Flow, Noise, and Vibration Effect on the Construction and Design of Low-Speed Wind Tunnel Structure. *Machines* **2023**, *11*, 360. [[CrossRef](#)]
66. Breuer, K.; Drela, M.; Fan, X.; Di Luca, M. Design and performance of an ultra-compact, low-speed, low turbulence level, wind tunnel for aerodynamic and animal flight experiments. *Exp. Fluids* **2022**, *63*, 169. [[CrossRef](#)]
67. Drela, M.; Huang, A.; Darmofal, D. Screened expanding turning-vane concept. *Exp. Fluids* **2020**, *61*, 75. [[CrossRef](#)]
68. Lindgren, B.; Johansson, A.V. Evaluation of a new wind tunnel with expanding corners. *Exp. Fluids* **2004**, *36*, 197–203. [[CrossRef](#)]
69. Lindgren, B.; Österlund, J.; Johansson, A. Measurement and calculation of guide vane performance in expanding bends for wind-tunnels. *Exp. Fluids* **1998**, *24*, 265–272. [[CrossRef](#)]
70. Bansmer, S.E.; Baumert, A.; Sattler, S.; Knop, I.; Leroy, D.; Schwarzenboeck, A.; Jurkat-Witschas, T.; Voigt, C.; Pervier, H.; Esposito, B. Design, construction and commissioning of the Braunschweig Icing Wind Tunnel. *Atmos. Meas. Tech.* **2018**, *11*, 3221–3249. [[CrossRef](#)]
71. Wallisch, J.; Hann, R. Design of a Low-Speed Icing Wind Tunnel for UAVs. In Proceedings of the Deutscher Luft- und Raumfahrtkongress 2020, Bonn, Germany, 14 September 2020. [[CrossRef](#)]
72. Talbi, M.; Duperrier, R.; Delestre, B.; Godard, G.; Brunel, M. Interferometric Ice Particle Imaging in a Wind Tunnel. *Optics* **2021**, *2*, 216–227. [[CrossRef](#)]
73. Gates, E.; Lam, W. Spray evolution in icing wind tunnels. *Cold Reg. Sci. Technol.* **1988**, *15*, 65–74. [[CrossRef](#)]
74. Cheng, N.S. Comparison of formulas for drag coefficient and settling velocity of spherical particles. *Powder Technol.* **2009**, *189*, 395–398. [[CrossRef](#)]
75. Bond, T.H.; Anderson, D.N. Manual of Scaling Methods. NASA/CR-2004-212875 2004. Available online: <https://ntrs.nasa.gov/citations/20040042486> (accessed on 16 June 2024).
76. Langmuir, I.; Blodgett, K. A Mathematical Investigation of Water Droplet Trajectories. *Atmos. Phenom.* **1946**, 335–347. [[CrossRef](#)]
77. *SAE Standard ARP5905*; Calibration and Acceptance of Icing Wind Tunnels. AC-9C Aircraft Icing Technology Committee, SAE Aerospace Recommended Practice (ARP), SAE International: Warrendale, PA, USA, 2015. [[CrossRef](#)]
78. Morel, T. Comprehensive Design of Axisymmetric Wind Tunnel Contractions. *ASME J. Fluids Eng.* **1975**, *97*, 225–233. [[CrossRef](#)]
79. *UNE 100716:2012*; Medición y Cuantificación de la Superficie Exterior de los Conductos de Aire de Chapa Metálica de Sección Rectangular. AENOR Asociación Española de Normalización y Certificación: Madrid, Spain, 2012.
80. *UNE 100717:2013*; Medición y Cuantificación de los Conductos de Aire de Chapa Metálica de Sección Circular y Oval. AENOR Asociación Española de Normalización y Certificación: Madrid, Spain, 2013.
81. *UNE-EN 12237:2003*; Ventilación de Edificios. Conductos. Resistencia y Fugas de Conductos Circulares de Chapa Metálica. AENOR Asociación Española de Normalización y Certificación: Madrid, Spain, 2003.
82. Soler&Palau Ventilation Group Cylindrical Cased Axial Flow Fans TGT Series Product Datasheet. Available online: <https://www.solerpalau.com/en-en/cylindrical-cased-axial-flow-fans-tgt-1051-serie/> (accessed on 30 June 2024).

**Disclaimer/Publisher’s Note:** The statements, opinions and data contained in all publications are solely those of the individual author(s) and contributor(s) and not of MDPI and/or the editor(s). MDPI and/or the editor(s) disclaim responsibility for any injury to people or property resulting from any ideas, methods, instructions or products referred to in the content.